Petroleum Science 22 (2025) 1080–1097

Contents lists available at ScienceDirect

Petroleum Science

journal homepage: www.keaipublishing.com/en/journals/petroleum-science

Review Paper

Unraveling key factors that influence and shape fluid flow dynamics in Brazilian salt Lagoon stromatolites: A case study in pre-salt analogues

Herson Oliveira da Rocha [a, b, c, *], Roseane Marchezi Missagia [a, d], Marco Antonio Rodrigues de Ceia [a, d], André Oliveira Martins [a, c], Rafaella Rocha Baggieri [c], Irineu de Azevedo Lima Neto [c], Victor Hugo Santos [a], Lucas Cesar Oliveira [c]

[a] Petroleum Exploration and Engineering Laboratory (LENEP), North Fluminense State University (UENF), Macaé, 27910-970, Rio de Janeiro, Brazil
[b] Polytechnic Institute (IPLOI), Campus Macaé, Federal University of Rio de Janeiro (UFRJ), Avenida Aluízio da Silva Gomes s/n, Granja dos Cavaleiros, Macaé, 27930560, Rio de Janeiro, Brazil
[c] Scientific Computing Supporting Foundation (FACC), Petropolis, 25651-075, Rio de Janeiro, Brazil
[d] National Institute of Petroleum Geophysics Science and Technology (INCT- Petroleum Geophysics), 40170-115, Salvador, Brazil

ARTICLE INFO

Article history:
Received 4 March 2024
Received in revised form
27 June 2024
Accepted 9 December 2024
Available online 18 December 2024

Edited by Meng-Jiao Zhou and Min Li

Keywords:
Fluid dynamics in stromatolites
Carbonate reservoirs
Numerical simulation
Pre-salt analogs

ABSTRACT

This study analyzes Brazilian stromatolites in Lagoa Salgada, serving as analogs for pre-salt rocks in the Santos and Campos basins. Despite their excellent petrophysical properties, such as high porosity and permeability, these reservoirs present challenges in fluid flow modeling and simulation. The research investigates various factors influencing the development of carbonate reservoirs, including diagenetic processes employing several techniques, such as microcomputed tomography (micro-CT) and digital rock physics (DRP), to study petrophysical and geological characteristics. Additionally, through numerical simulations, the properties of fluid flow in different microfacies of stromatolites are estimated, with particular emphasis on understanding and highlighting changes in the direction of fluid flow in the three characterized microfacies. These findings offer crucial insights into optimizing oil and gas exploration and production techniques in carbonate reservoirs, providing a comprehensive understanding of the dynamics of fluid transport in porous media, especially in terms of directional changes within stromatolites.

1. Introduction

Since large hydrocarbon reserves were found in lacustrine and Lagoon carbonate systems in the Santos and Campos basins, pre-salt zone carbonate reserves are becoming more and more interesting to research. Scientists are interested in learning more about the development and properties of these reservoirs, which are found beneath Aptian evaporites (Abrahão and Warme, 1990; Carminatti et al., 2009; Saller et al., 2016; Ceia et al., 2022).

Various factors, including hydrological conditions, sedimentary input, temperature variations, and water geochemistry, influence carbonate reservoir formation. These factors contribute to developing different pore systems and pore types, leading to heterogeneity in marine and continental carbonate reservoirs (Choquette and Pray, 1970; Lønøy, 2006; Ahr, 2008). Additionally, some diagenetic processes including dissolution, precipitation, and fracturing, directly impact the permoporous system of the carbonate rock and are critical for interpreting the petrophysics data of the microbialites under study (Ehrenberg et al., 2006, 2012; Chafetz, 2013; Brigaud et al., 2014).

Furthermore, there are control factors and mechanisms that contribute to the geologically long-term preservation of pores and must be taken into consideration, such as a hard dolomitized microbiological framework, a lack of mineral cementation due to fluid flow, a petroleum charge, and eventual pyrobitumen coating, and high concentrations of CO_2 and H_2S from organic diagenesis and TSR, according to Zhu et al. (2020).

Researchers have employed various techniques to study the petrophysical and geological characteristics of carbonate reservoirs. For instance, Proctor et al. (2019) examined petrophysical qualities in stromatolites from the Lagoa Salgada (Holocene) and Codó

* Corresponding author.
E-mail address: herson.rocha@mace.ufrj.br (H. Oliveira da Rocha).

https://doi.org/10.1016/j.petsci.2024.12.009

Formations (Aptian) through subsampling growth structures and utilizing microcomputed tomography (CT).

Similarly, Brelaz et al. (2017) used analogous rocks from outcrops to forecast the petrophysical and geological properties of underground reservoirs, aiming to understand the permo-porous conditions of microbial limestones in the pre-salt section. They compared the lithofacies and depositional circumstances of these rocks with those of pre-salt carbonate reservoirs.

Ricardi-Branco et al. (2018) characterized contemporary and extinct microbial biofacies in the Holocene Lagoa Salgada, focusing on the interactions between metazoans and microbial communities and their influence on microbialite morphology. X-ray microtomography and petrological thin section investigations were utilized to describe the microtextures of different biofacies. Similarly, Silva et al. (2018) conducted a petrographic study on stromatolites from Lagoa Salgada to map their various forms and identify potential risks, contributing to geoconservation efforts.

Oliveira et al. (2022) employed laboratory measurements and numerical simulations from digital rock physics to evaluate elastic anisotropy in coquinas from the Morro do Chaves Formation, which serves as a Brazilian pre-salt analog. By estimating elastic moduli and wave velocities, they aimed to gain insights into the rock's properties.

Ceia et al. (2022) evaluated the porosity, pore size distribution, surface area, tortuosity, permeability, and pore compressibility of these stromatolites using mercury intrusion porosimetry (MIP) data. These findings allowed for a comparison with pre-salt reservoir data and shed light on the pore system of these rocks. This comparison showed that the pre-salt stromatolites from Brazil exhibit similar permo-porosity and pore compressibility tendencies to those of the two facies of these outcrop rocks.

Soltanmohammadi et al. (2024) investigated the petrophysical properties, oil recovery factor, and fluid movement patterns in stromatolite samples from Lagoa Salgada. They categorized the samples into vugular and fine-grained types based on the average pore size and conducted core flooding experiments coupled with CT scans to analyze the absolute permeability and flow patterns. This research aimed to understand the permeability difference and flow pattern contrast between these two types of composite rock samples.

This study uses numerical simulations and predictive analysis techniques to estimate the flow velocity and permeability in three microfacies (A, B, and C) of the stromatolite of Lagoa Salgada based on work by Archilha et al. (2013) and Ceia et al. (2022). This stromatolite is considered an analog to pre-salt rocks, and we use digitized rock structures obtained from high-resolution computed tomography (μCT) as input data for their simulations.

The study aims to provide insights into the fluid transport properties of these types of rocks, which can be useful for understanding fluid flow in carbonate reservoirs and improving oil and gas exploration and production techniques. The uniqueness of this study consists in the analysis of the impact of petrophysical properties, including the geometric properties of the porous system (aspect ratio, gamma, pore size diameter) on microfacies (A, B, and C) and their impacts on the change in flow direction.

2. Geological and petrophysical characterization

2.1. Santos and Campos basin

The Santos Basin is located between parallels 23°S and 28°S, covering an area of approximately 350,000 km^2; it is limited to the north by the Campos Basin through the Cabo Frio Arc and to the south by the Pelotas Basin through the Florianópolis Platform. The Campos Basin is located between the northwest coast of Rio de Janeiro and the southeastern state of Espírito Santo and between parallels 21°S and 23°S. It is limited to the north by the Vitória Arc and to the south by the Cabo Frio Arc, and it has an extension of approximately 100,000 km^2. This region includes the main exploratory blocks and oil production fields within the pre-salt polygon (Fig. 1).

Both basins are passive margin basins that were generated in an extensional tectonic regime during the breakup of Gondwana. The rift system that formed led to the opening of the South Atlantic (Jurassic-Early Cretaceous) (Rabinowitz and LaBrecque, 1979; Austin Jr and Uchupi, 1982; Nürnberg and Müller, 1991; Cainelli and Mohriak, 1999).

Carbonate rocks in both basins were deposited before the evaporitic strata (lower Albian), also known as pre-salt carbonates, and they were generated during rift and post-rift phases (Barremian-Aptian stages) (Moreira et al., 2007; Winter et al., 2007). The rift phase is characterized by lithospheric extension and asthenospheric uplift, which resulted in deep lakes that were filled by volcanic and sedimentary rocks (Lima and De Ros, 2019; De Oliveira et al., 2019; Chinelatto et al., 2020; Chinelatto et al., 2021; Sternai et al., 2021; Korchinski et al., 2021). The sag phase represents a stage of clastic, carbonatic, and magnesian clay deposition, the deposits of which further overlapped with evaporitic sequences generated in arid conditions with marine incursions (Thompson et al., 2015; Alvarenga et al., 2021).

The main constituents of the pre-salt rocks of the rift phase are bivalves, low-energy ooids, ostracods, and gastropods, in order of abundance. In the sag phase of the basin, the representative components in order of abundance are spherulites, shrubs, carbonate intraclasts, clay minerals, clay intraclasts, and low-energy ooids.

The Santos Basin was divided by Moreira et al. (2007) into three stratigraphic supersequences: rift, post-rift, and drift. The Itapema (Jiquiá age) and Barra Velha (Alagoas age) formations encompass carbonate (Guaratiba Group) deposits that were deposited before Albian evaporites. The Itapema Formation (K38 sequence) was deposited in a lacustrine environment during the rift sequence. This formation is characterized by wackestones, bioclastic grainstones, and packstones. In the distal regions, both siliciclastic and carbonatic shale layers with organic matter occur, as well as sandstones and conglomerates. Both biostratigraphic and chronostratigraphic data indicate that this formation is correlated with the Coqueiros Formation deposits in Campos Basin (Moreira et al., 2007).

The Barra Velha Formation (sag/postrift sequence), with stages K44, K46, and K48, consists of stromatolites, microbial laminites, talc-rich microbialites, magnesian clays, and carbonate shales from a restricted Lagoon environment with shallow and probably alkaline waters. This unit is equivalent to the Macabu Formation of the Campos Basin, according to biostratigraphic and chronostratigraphic data (Fig. 2).

The Campos Basin sediment records are divided into three tectonic phases, namely, rift, post-rift, and drift, as described by Winter et al. (2007). Pre-salt carbonate rocks from this basin are the Coqueiros Formation (Jiquiá) and Macabu Formation (upper Alagoas). Both formations are included in the Lagoa Feia Group (Winter et al., 2007). The Coqueiros Formation consists mainly of bioclastic rudstones and grainstones, usually called “coquinas”, and were deposited in a high-energy lacustrine environment during the rift phase. The bioclastic Coqueiros deposits (K38 sequence) are predominantly composed of bivalve mollusks, with minor concentrations of gastropods and ostracods.

Winter et al. (2007) described the Macabu Formation (K46 and K48 sequences) as laminated microbial and stromatolite deposits that are dolomitized and/or silicified, with rare sandy and shale intercalations that were deposited in a restricted Lagoon

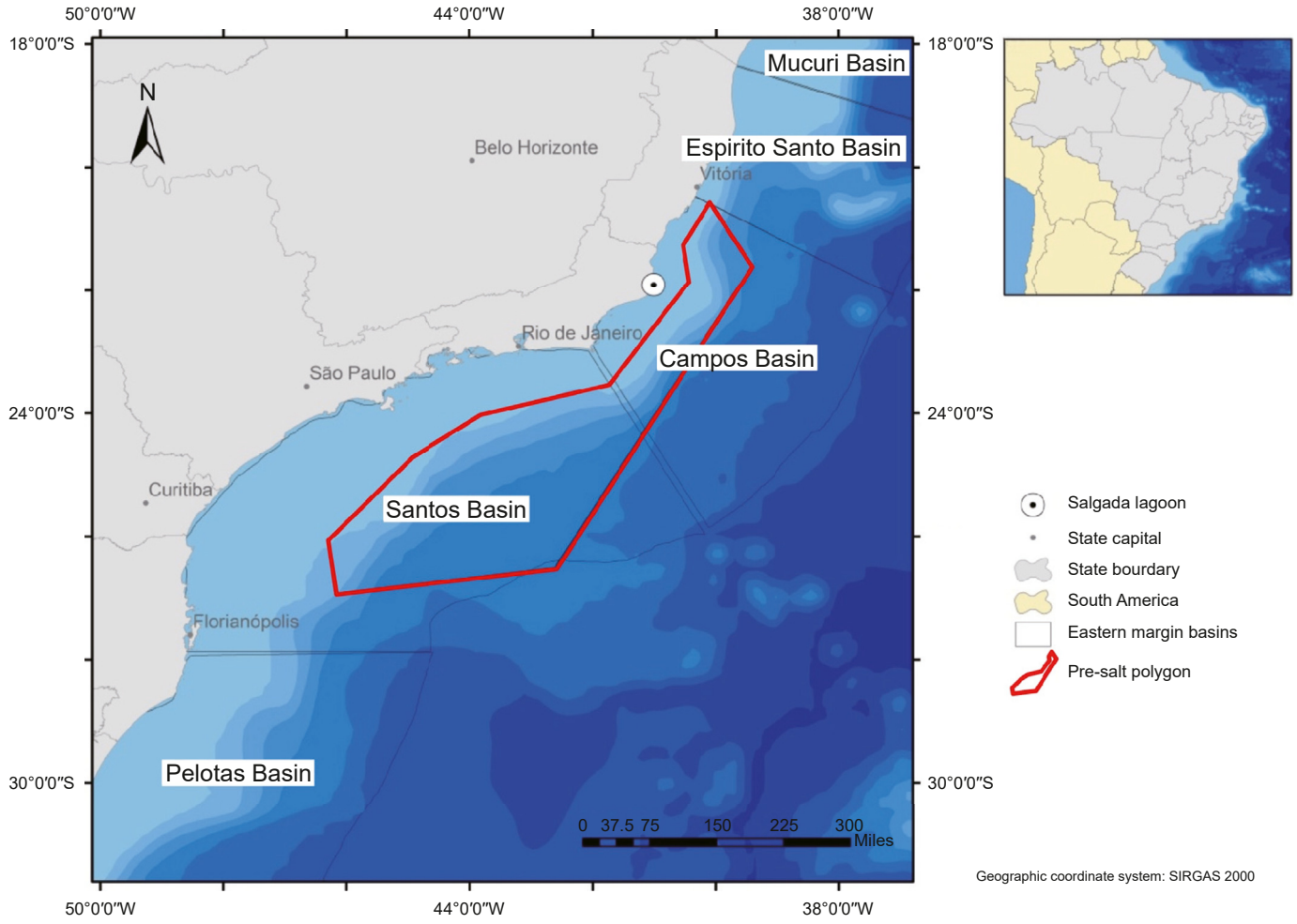

Fig. 1. Location map of the pre-salt polygon from Santos and Campos basins, and the location of a stromatolite analog, Lagoa Salgada (white point) (modified from Herlinger Jr et al. (2020)).

environment (sag phase), according to Fig. 2. The Macabu Formation was recently interpreted as a chemical deposit controlled by the alkaline lacustrine water composition (Wright, 2012; Wright and Barnett, 2015).

2.2. Lagoa Salgada quaternary analog

The Lagoa Salgada (a highly saline Lagoon) occupies an area of approximately 16 square kilometers near the coastal town of the Cape of São Tomé of the municipality of Campos, which is on the north coast of the state of Rio de Janeiro (Brazil); the Lagoon contains the unique occurrence of recent columnar carbonate stromatolites from all over Brazil and probably from South America (Fig. 3).

The geological history of the Lagoon is intimately associated with sea level fluctuations during the late Quaternary and the formation of the Paraiba do Sul River delta. The stromatolites occur in discontinuous patches, principally at the southwest and northwest borders of the lake, overlying marine sands, and are normally covered by soil or water during high tides. The thickness of stromatolite bioherms and biostromes varies along the western border. The discrete columnar stromatolites present great vertical variations (Srivastava et al., 1999).

According to Rezende et al. (2013) and Brelaz et al. (2017), the porosity and permeability of Lagoa Salgada stromatolites show a wide variation, ranging from 5% to 41% and from 0.02 to 46,000 mD, respectively. The analysis also indicates that 30% (relative frequency) of samples have porosity levels between 20% and 25%, while 45% exhibit permeability values between 100 and 1000 mD (Fig. 4).

2.3. Macroscopic analysis

Based on the facies classification proposed by Gerdes et al. (1993) for microbial mats and by Riding and Liang (2005) and Riding (2011) for stromatolites and thrombolites, three facies were identified in this research: microbial mat, thrombolite, and thrombolitic/vugular stromatolite. Textural characteristics, structure (presence or absence of macrolaminations), bioerosion, and pore types (vugular or fenestral) were used as criteria to distinguish these facies. However, as only one sample was available, a detailed analysis could not be performed. The top of the stromatolite was sampled, and two possible facies were identified (Fig. 5).

Overall, the variation in pore size distribution and the nature of the facies significantly impact fluid flow behavior in the Lagoa Salgada stromatolites. Microfacies with high porosity and good connectivity, such as microfacies B, facilitate efficient flow, while microfacies with limited porosity or discontinuities, such as microfacies A and some portions of microfacies C, can act as barriers, reducing flow efficiency and creating stagnation zones.

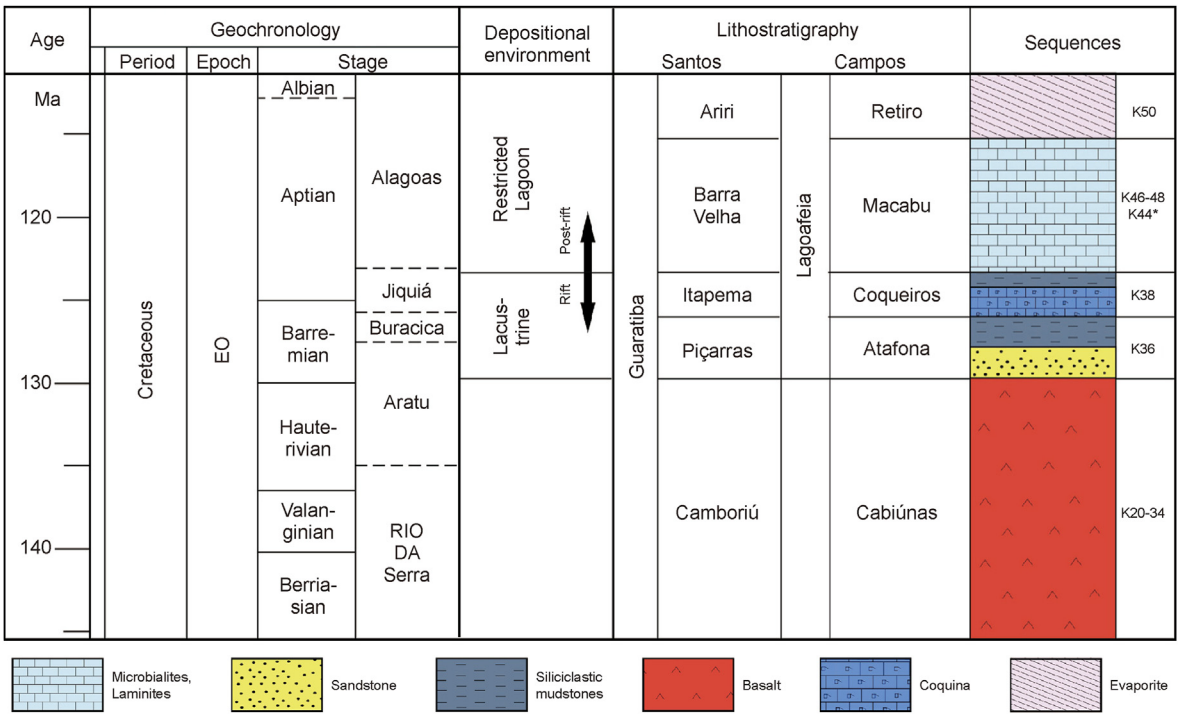

Fig. 2. Stratigraphic chart for the Lower Cretaceous of the Santos and Campos basins. The chart shows a simple lithology for each formation, see the text. Itapema, Barra Velha, Coqueiros and Macabu formations are the focus of this research. K44* is a specific sequence of Barra Velha Formation (Santos Basin) (modified from Moreira et al. (2007) and Winter et al. (2007)).

Fig. 3. Overview of the outcrop Lagoa Salgada stromatolites.

2.3.1. Microbial mat (facies A)

This facie represents the base of the sample. It has a thickness of 4 cm and shows alternating gray to light brown laminations. The light laminations are composed of carbonate material, while the dark laminations are composed of siliciclastic material (predominantly quartz). Facies with subplanar/wavy lamination occur as small-scale stratiform intercalations. Serpulidae tubes and microgastropods are present. Fenestral porosity is the dominant pore type, and in some portions, vugular porosity occurs. The gradation from Facies A to Facies B is abrupt.

2.3.2. Thrombolite (facies B)

The thickness of these facies is 3 cm. Its color is brown and, in some portions, reddish. The structure is formed by clots, and the surrounding cavities are interconnected. This is the most porous portion of the sample, and the cavern is the predominant porosity. Microgastropods are present. The gradation from Facies B to C is abrupt.

2.3.3. Thrombolytic/vugular stromatolite (facies C)

This type is present at the top of the sample, with a more rounded shape and colors ranging from light brown to yellowish. The base is sandier, while the top is siltier. Its thickness is approximately 10 cm. The structure is diffuse, and in its upper portion, there are microcolumns with incipient laminations. The predominant porosity is vugular, and in some portions, there is moldic porosity (microgastropods).

3. μCT data analysis

Digital image analysis (DIA) principles and best practices can be applied to a variety of earth science disciplines. DIA is a multidisciplinary technique for computing rock parameters (such as porosity, permeability, formation factors, water saturation curves, capillary pressure curves, resistivity index, and relative permeability) and describing microstructural qualities using high-resolution images (such as X-ray computerized tomography and scanning electron microscopy) (Tsuchiyama et al., 2011; Tahmasebi et al., 2016; Saxena and Mavko, 2016; Saxena et al., 2017, 2018, 2019; Kong et al., 2018; Da Wang et al., 2019).

Laboratory measurements remain the industry standard due to their simplicity and availability. Many businesses routinely conduct conventional core analyses in their labs without significant issues. However, digital rock analysis becomes particularly valuable in situations where core data is unavailable or when dealing with friable materials, low-porosity samples, and other challenging conditions.

The most crucial stage in simulating rock properties (such as

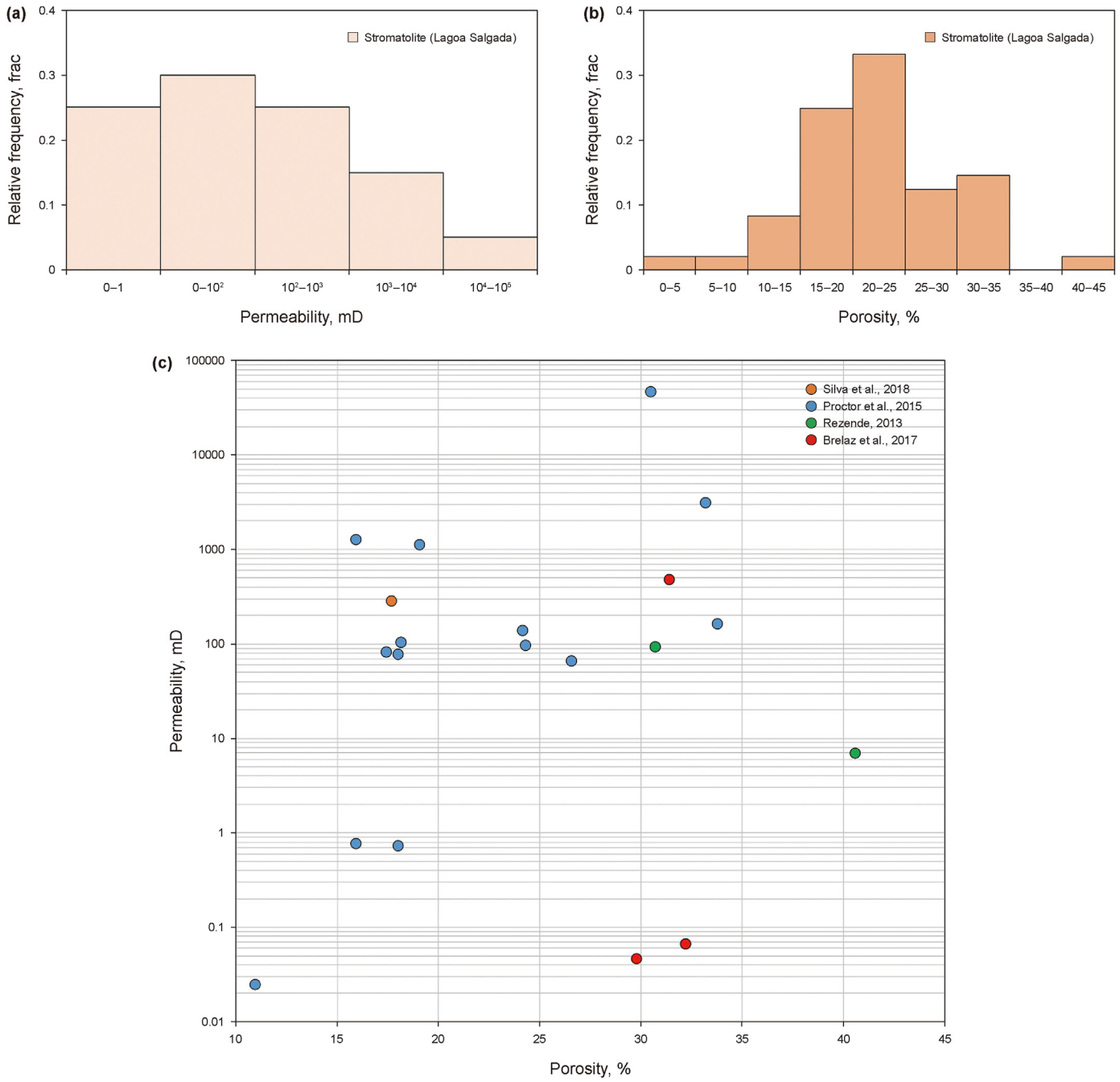

Fig. 4. Petrophysical properties of Stromatolites from Lagoa Salgada. Histograms for the porosity and permeability of stromatolite samples **(a)** porosity, **(b)** permeability, highlighting some statistical parameters, and **(c)** plot of porosity versus permeability.

permeability, elasticity, and electrical conductivity) is to compare the numerical solver to a known truth, such as analytical reference solutions or previously calculated rock property standards, which must be independently validated.

Several studies have examined DIA benchmarks, but they have been limited to a small number of rock microstructures and properties computed using only a few numerical solvers. Additionally, there were no numerical solutions for idealized microstructures with properties comparable to known analytical solutions. Comparing these numerical solutions to analytical ones allows researchers to establish the limits of specific numerical solvers (Saxena et al., 2017; Alpak et al., 2018).

4. Materials and methods

Initially, we employed 3D image volumes previously acquired using an X-ray imaging beamline (IMX) facility through an academic project established with the Brazilian Synchrotron Light Laboratory (LNLS) of the Brazilian Center for Research in Energy and Materials (CNPEM), and the images were processed for this research. The apparatus comprises a synchronized energy distribution (4–20 keV), and the experiments were performed using 10× optical magnification, an image field of 1.68 × 1.68 mm, and a voxel resolution of 0.82 μm.

A total of 3 tomography images were acquired, and the

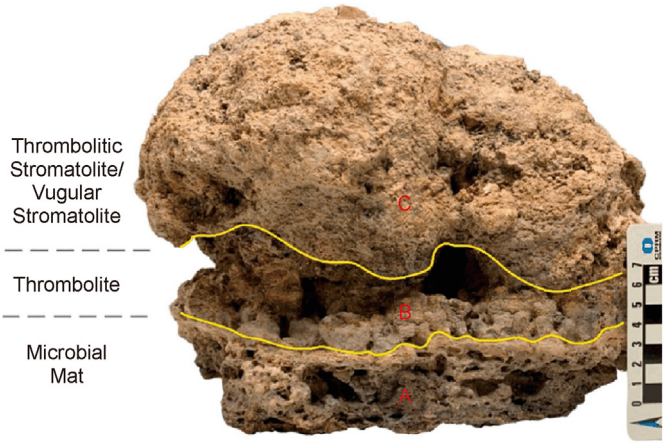

Fig. 5. Facies are defined in the Lagoa Salgada stromatolite through textural and structural characteristics. The classification of facies was based on Gerdes et al. (1993), for microbial mat, and Riding (2011), for stromatolite and thrombolite.

stromatolite rock samples were prepared, with sizes between 0.9 and 1.2 mm in diameter, under the image field limit. Data acquisitions were performed for each sample, and the respective 3D volumes were reconstructed by the following main steps: i) rotation axis correction; ii) gain, border scattering, and ring correction; ii) brightness and contrast adjustment; and iv) data saving using an 8-bit grayscale with dimensions of 2048 × 2048 × 2048 voxels. Acquisition details are shown in Fig. 6.

Although there is a large textural, structural, and petrophysical variation between facies A, B, and C, within the same facies the variation is smaller since it was formed under the same conditions. To ensure the representativeness the samples were taken from the most dominant portions of each facies according to textural, structural, and porosity characteristics.

The FlowDict module of GeoDict software simulates virtual flow experiments and analyzes the data to forecast effective material properties in which the flow experiment requires three sets of input parameters: a three-dimensional representation of a structure; a Newtonian fluid (gas or liquid with a constant viscosity); and the experimental processes parameters, such as flow velocity and flow direction (Saxena et al., 2017, 2018, 2019; Da Wang et al., 2019; Schmidt et al., 2019).

In this simulation, two types of experiments were performed: mean flow velocity prediction for a given pressure drop and pressure drop prediction for a given mean flow velocity. Darcy's law calculated the material permeability utilizing the mean flow velocity, fluid viscosity, pressure drop, and media thickness in a post-processing step (Wiegmann et al., 2010; Schmidt et al., 2019).

The linear relation between the velocity and pressure through a porous medium is described by Darcy's law, which describes the linear relationship between the velocity and pressure across the porous medium. Darcy's law describes the flow of a fluid substance through a porous medium. This flow is defined by

$$\mu u = K \nabla p, \tag{1}$$

where u, p, μ, and K describe the velocity, pressure, and dynamic viscosity constant and a tensor of permeability, respectively.

The effective permeability of a representative periodic volume element in the three-dimensional case is described by the tensor $K \in \mathscr{P}_{3\times3}$. The tensor K can be determined by applying three-axis

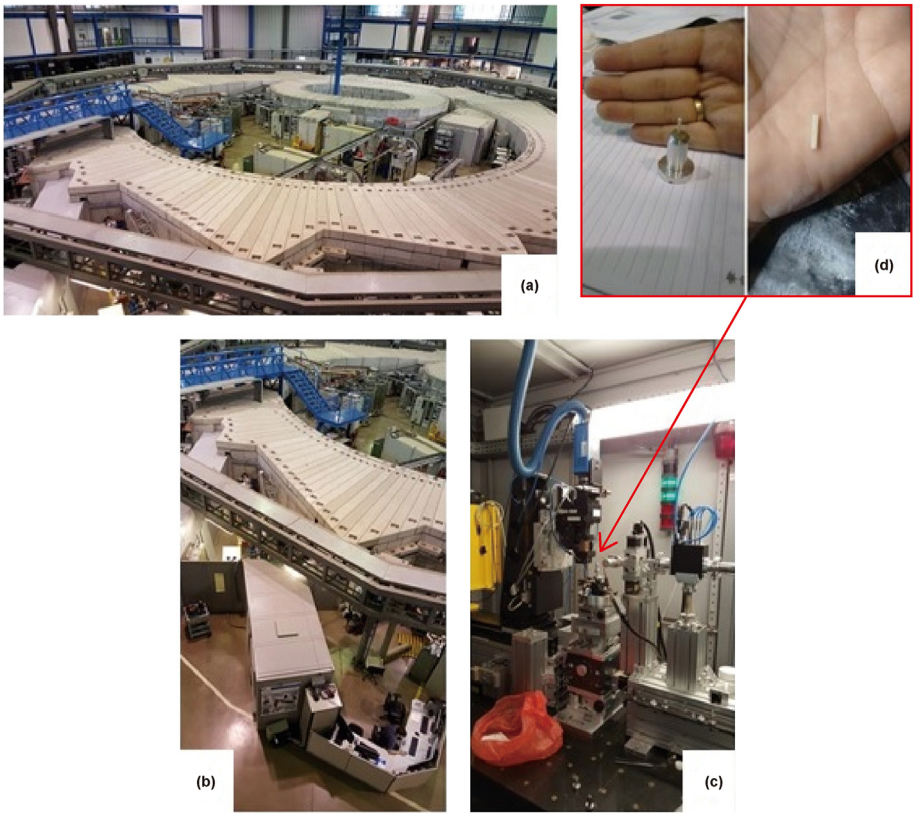

Fig. 6. Schematic summary of the acquiring X-ray computed tomography data. Internal view of the Brazilian Synchrotron Light Laboratory **(a)**, X-ray imaging beamline **(b)**, PCO-2000 white beam microscope **(c)**, and highlighting the sample size **(d)**.

aligned pressure drops and evaluating the corresponding mean velocity. Darcy's law is used to calculate the structure's permeability tensor for flow permeability in the following way:

$$\overrightarrow{u^i} = -\mu^{-1}\begin{pmatrix} K_{xx} & K_{xy} & K_{xz} \\ K_{yx} & K_{yy} & K_{yz} \\ K_{zx} & K_{zy} & K_{zz} \end{pmatrix} \nabla p^i \tag{2}$$

Here, $\overrightarrow{u^i}$ is the averaged velocity vector (averaged flux with $i = 1$ corresponding to a pressure drop in the X-direction, $i = 2$ corresponding to a pressure drop in the Y-direction and $i = 3$ corresponding to a pressure drop in the Z-direction) and is the pressure gradient (or pressure difference) in the i^{th} direction. $L^1 = NX \times L_v$, $L^2 = NY \times L_v$, and $L^3 = NZ \times L_v$ are the physical lengths of the computational domain in the directions of interest. L_v is the physical length of a voxel, and NX, NY, and NZ are the numbers of voxels in the three coordinate directions (X, Y, and Z).

$$\nabla p^i = \frac{\Delta p^i}{L^i}, \text{ with } \Delta p^1 = \begin{pmatrix} 2 \\ 0 \\ 0 \end{pmatrix}, \Delta p^2 = \begin{pmatrix} 0 \\ 2 \\ 0 \end{pmatrix}, \Delta p^3 = \begin{pmatrix} 0 \\ 0 \\ 2 \end{pmatrix} \tag{3}$$

Nonzero off-diagonal entries (Eq. (2)) indicate that the calculation produced a flux in directions perpendicular to the applied pressure drop direction. This is due to directional anisotropies of the structures and the lack of boundaries that could stop the flow in the perpendicular directions (in contrast to experiments where boundaries are usually present) (Wiegmann et al., 2010; Linden et al., 2015).

Darcy's law comes with two caveats: Darcy's law holds true only for extremely slow (creeping or Stokes) flows with a Reynolds number of zero (Abe, 2017; Coleman et al., 2018). In this regime, changing the pressure drop or velocity by a factor alters the other by the same factor, ensuring that Darcy's law predicts the same permeability value every time.

One of the key factors influencing fluid flow in porous media, especially vuggy porous media, is the Reynolds number (R_e). The Reynolds number illustrates the relationship between inertial and viscous forces and aids in the identification of a flow regime. Generally speaking, Reynolds number divides the flow regime into two separate sections. When the Reynolds number is less than 2000, laminar flow occurs. Conversely, a flow regime with a Reynolds number higher than 2000 is referred to as turbulent flow (Simões Maciel et al., 2019; Soltanmohammadi et al., 2024).

Eq. (4) displays Reynolds number equation, where ρ is fluid density in kg/m^3, v is Darcy's velocity divided by porosity ($v = u/\varphi$) in m/s, d_p is the median grain size of the porous media as a proxy for characteristic pore length in m, and finally μ is fluid viscosity in kg/m·s (van Lopik et al., 2017; Faroughi et al., 2022; Soltanmohammadi et al., 2024). The Reynolds calculated for microfacies A, B, and C were 817, 860, and 705, respectively.

$$R_e = \frac{\rho v d_p}{\mu} = \frac{\text{inertial force}}{\text{viscous force}} \tag{4}$$

Since the fluid's viscosity is written separately in our formulation of Darcy's law, permeability is a true material property. Instead of pulling the viscosity into the definition of permeability, the viscous resistivity is considered, i.e., the quotient of fluid viscosity and material permeability. Thus, if quantities such as water or air permeability are needed, the reciprocal of the viscous resistivity is considered. Defining permeability as a material property also means that the pressure drop cannot be so high as to result in the deformation of the media (Linden et al., 2018).

The second caveat lies in the definition of length L in Darcy's law. This length is not designed to include the inlet and outlet (inflow and outflow regions) that some virtual flow experiments require. Under the assumptions of slow flow and a void of the inlet and outlet, choosing the Stokes flow and using the computed permeability is valid. Faster flows are described by the Navier-Stokes equation (Coleman et al., 2018).

For such flows, the relation between pressure drops and the mean velocity is not linear. Even for the Navier-Stokes method, all experiments assume a steady flow regime, i.e., do not allow for time-dependent behavior such as turbulence. In practice, this means that the velocity and pressure drop cannot be arbitrarily high, and it is advised to carefully examine the validity of predictions for their own application area (Wiegmann et al., 2010; Mahmoud and Zabihi, 2017; Linden et al., 2015; Zhang et al., 2019; Lv et al., 2021).

Among many applications, computations can be used to determine air and water permeabilities in DIA, to study gas and liquid permeabilities and pressure drops in filter media, to predict gas permeability for the extraction of gas in reservoirs and source rocks, and to predict the flow characteristics of hydrocarbons in oil and gas reservoirs (Wiegmann et al., 2010; Lima Neto et al., 2018; Schmidt et al., 2019).

In the workflow simulation, two solution methods (solvers) are offered to meet the needs of the equations defining fluid flow. The explicit jump (EJ) solver is quick and requires little memory, but it can be utilized only when the pressure drop/flow velocity relationship is linear. The explicit finite volume (EFV) solver takes longer to converge and requires more computational memory, but it can handle nonlinear fluid flow (Wiegmann et al., 2010; Schmidt et al., 2019).

The explicit jump (EJ) solver and the explicit finite volume (EFV) solver can both compute slow fluid flow that follows the Stokes equation. The explicit finite volume (EFV) solution is needed for faster flows approximated by the Navier-Stokes equations.

The flow velocity fields are calculated by the selected flow solver in the three directions by setting up the pressure drop in the physics parameters and selecting the computation directions in the solver options. The default values correspond to the virtual pressure drop of 500 psi across the structure in the z-direction. The x- and y-directions can also be selected so that the flow is calculated in those directions (Fig. 7).

For the linear Stokes EJ and Stokes EFV flow solvers, this description yields a permeability tensor K that is independent of the applied pressure drop, as well as from the fluid viscosity that is used. Thus, permeability is considered a material property. The Navier–Stokes model for the EFV flow solver is a nonlinear method. Hence, $\overrightarrow{u^i}$ is no longer proportional to ∇p^i. In the nonlinear case, the computed velocities are typically lower than in the linear case. In this case, the permeability tensor K depends on the pressure drop and the viscosity, and thus, it is not a material property.

The FlowDict module computes incompressible, stationary flows of Newtonian fluids. The solvers compute the local velocity field and pressure distribution in pores. In this case, the LIR solver, which solves the Stokes-Brinkman equation, is used (Wiegmann et al., 2010).

The Stokes equations are a simplified version of the Navier–Stokes equations. When the fluid velocity is very slow, i.e., when the Reynolds number is low, they are utilized. Temperature is not taken into account, and a constant density is assumed. As a result, we must consider the fluid's pressure and velocity. We also limit ourselves to the steady-state situation, in which there is no unstable acceleration. The convective acceleration is also omitted in the formulation (Linden et al., 2015). The Stokes equations are then defined by

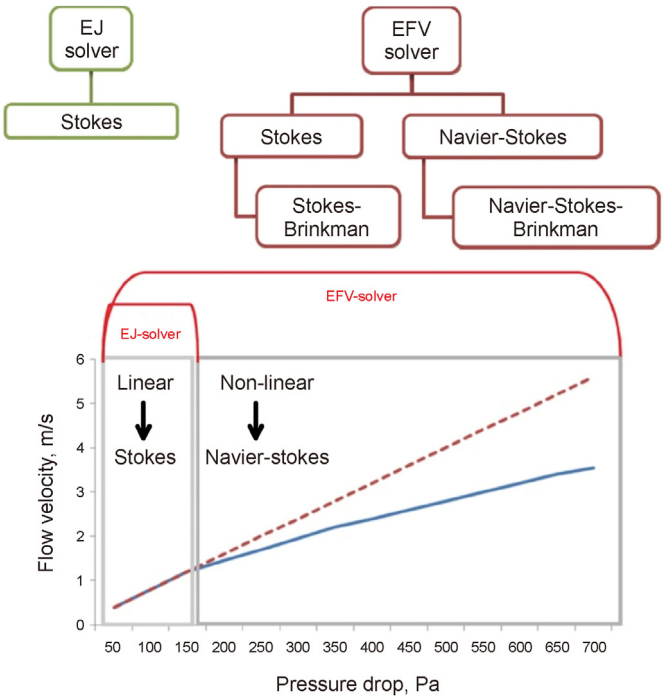

Fig. 7. A brief comparison between the Explicit Jump (EJ) and Explicit Finite Volume (EFV) solutions and their relationship with Stokes and Navier-Stokes equations for modeling slow and fast flows (above) and the relationship between pressure drop vs. flow velocity for each solver, based on the flow type linear or nonlinear (below) (modified from Wiegmann et al. (2010)).

$$\mu\nabla u - \nabla p = 0, \quad \text{momentum conservation} \tag{5}$$

$$\nabla u = 0, \quad \text{mass conservation} \tag{6}$$

$$u_{|\partial u,\partial p} = 0, \quad \text{no slip condition} \tag{7}$$

To reduce the duration of the simulations, the images of microfacies A, B, and C were cut to a smaller size before starting the numerical simulation. In this step, we used a subvolume of the samples, with dimensions of 250 × 250 × 250 voxels, obtained from the central region of the samples of each microfacies. Using the threshold tool, which separates the image according to the gray level of each voxel, the image was then segmented into a binary image (pores + rock matrix).

Following the acquisition of 2D thin sections, images were saved as 24-bit RGB files. Employing Fiji-ImageJ software and the GeoDict toolset, the images underwent the following process: initial image preprocessing to create paletted 8-bit files suitable for Fiji-ImageJ loading. The segmentation process initiated by porosity thresholding was guided by a technician to achieve optimal distinction between grains and pores.

Manual intervention was necessary, as automatic threshold algorithms such as the Otsu method (Otsu, 1979) struggled with identifying the highlighted pore space. This resulted in the creation of binary images. Porosity and related geometric properties relevant to digital image analysis (DIA) parameters were computed. The segmentation phase aimed to effectively differentiate between the matrix and pore space for accurate property analysis and estimation (Lima Neto et al., 2018).

For this, we use the watershed segmentation algorithm, which is a method to detect and separate pore bodies in 2-D or 3-D images. Consider two objects touching, as in Fig. 8(a). The goal is to detect and separate these connecting objects using the watershed segmentation algorithm. In the first step, the distance transform should be applied to the binary image (Fig. 11(a)) to generate the distance map (Fig. 8(b)).

The brightness of a pixel in distance transformation is determined by the distance between that point and the nearest pixel of the object boundary (Fig. 8(b)) (Rabbani and Ayatollahi, 2015; Rabbani et al., 2016). The next step is to create a topological surface based on the distance map (Leavline and Singh, 2014). The deeper parts of the formed surface represent brighter pixels (Fig. 8(c)).

Consequently, for each of the objects that are touching in the image, a basin is created. In the watershed algorithm, we suppose that rain falls over the two basins. Water is gathered in the deepest part of the basins according to the depth contours (Fig. 8(d)). When flooding advances, the level of water moves upward in the basins until the two isolated water pools touch each other.

The pixels in which the watershed of the two basins reach each other are known as the watershed ridgeline. By continuing the flooding, all points of the watershed ridgeline are detected. The watershed ridgeline separates the two touching objects (Fig. 8(e)), each of which are labeled as a pore body (Rabbani and Ayatollahi, 2015; Rabbani et al., 2016). Next, by checking the pore boundary pixels, the connected pore bodies are detected. The resulting pore network can be shown using the ball-and-stick model (Fig. 8(f)).

Importantly, X-ray diffractometry (XRD) revealed that the three microfacies are composed of the same minerals but in different proportions. The two upper portions (A and B) are mainly composed of high molar-concentration magnesian calcite (CMAC), with approximately 10 mol% $MgCO_3$ (a value obtained by the Rietveld method) and smaller amounts of quartz and aragonite (Archilha, 2015; Archilha et al., 2016).

With the XRD data obtained for the three microfacies, it was possible to classify them according to their mineralogical composition (Table 1). Rocks that have more than 50% carbonate minerals in them are classified as carbonates, according to the commonly accepted classification provided by Leighton and Pendexter (1962). Lagoa Salgada stromatolitic facies meet this description.

On the other hand, the lower portion C is composed of >53% quartz, with a high occurrence of CMAC (44.5%). The concentration of quartz in the stromatolitic head increases with depth; that is, microfacies C, which underwent marine influence during its formation, presents the highest concentration of this mineral. Already, the concentration of magnesian calcite follows an inverse trend: it is present in a greater amount in microfacies A (~85%), and gradually decreases until the occurrence of ~45% in microfacies C (Archilha, 2015).

Fig. 9 shows the digital core analysis workflow employed in this research, which consists of imaging (μCT), image processing and segmentation, digital rock computations, and relative permeability analysis.

Bulk and grain densities were estimated through gas porosimetry using UltraPore 300 equipment. Bulk density was determined by the dry weight and bulk volume ratio, while the grain density can be estimated using Eq. (8) (Asquith and Gibson, 1982). In this model, based on the mineralogical composition of the material, as shown in Table 1, which shows the material information of the stromatolite for simulation, the sample has a density of 2.516 g/cm^3, which was obtained according to Table 2.

$$Rho_b = Rho_g - (Rho_g - Rho_{air})*\varphi, \tag{8}$$

where Rho_b is the bulk density, Rho_g is the grain density, Rho_{air} is the air density, and φ is the porosity.

The geomechanical properties utilized included Young's modulus of 19.3 GPa, a Poisson's ratio of 0.3, an effective bulk

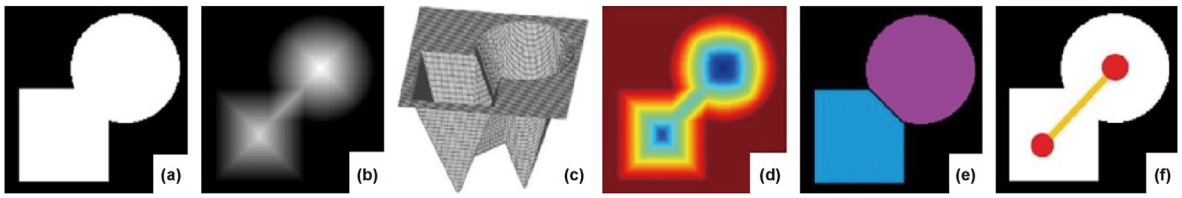

Fig. 8. Sample segmentation using the watershed method: **(a)** the original binary image, **(b)** the grayscale distance map, **(c)** topological surface, **(d)** depth contours, **(e)** detected objects separated by watershed ridgeline, and **(f)** ball-and-stick model (modified from Rabbani and Ayatollahi (2015) and Rabbani et al. (2016)).

Table 1
Mineralogical composition (in %) of the three stromatolitic facies used in the classification of the lithology type (adapted by Archilha (2015); Leighton and Pendexter (1962)).

Microfacies	Calcite Mg + Aragonite	Non-Carbonates	Dolomite	Type lithology
A	90.3	9.7	0.0	Limestone
B	65.5	30.5	0.0	Limestone (impure)
C	44.5	53.5	0.0	Non-carbonate

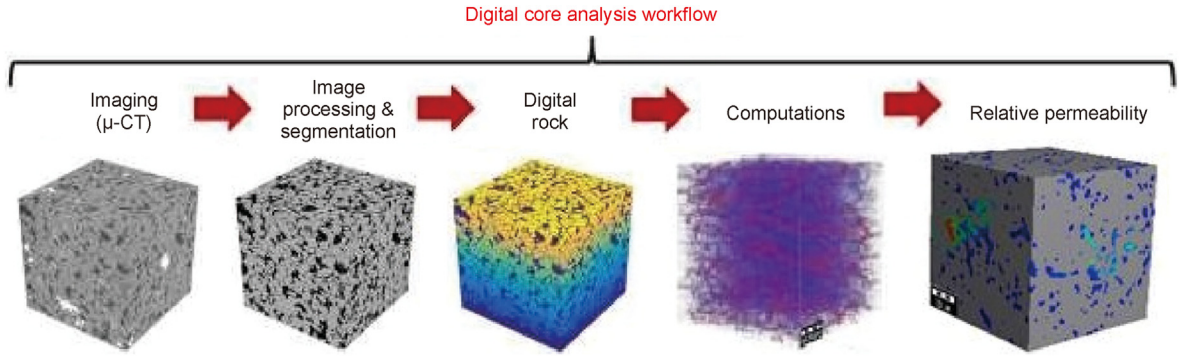

Fig. 9. Digital rock analyses workflow (modified from Saxena et al. (2017)).

Table 2
Results of porosity and grain density obtained by ultra pore-300.

Stromatolite sample (SSL-1)		
Porosity, %	Grain density, g/cm^3	Bulk density, g/cm^3
38.573 ± 1.15	2.516	1.545

modulus of 16.033, and an effective shear modulus of 7.42308, respectively. These parameters were calculated based on studies by Hashin-Shtrikman (Brown, 2015). The fluid properties were as follows: density of 1.2 kg/m^3, dynamic viscosity of 1.834.10^{-5} kg/m·s, and kinematic viscosity of 1.52325.10^{-5} m^2/s (Tropea et al., 2007); these values were available in the GeoDict library. A pressure drop of 500 psi and an air temperature of 25 °C were assumed based on Archilha (2015).

5. Results and discussions

The use of the FlowDict module determines whether permeable materials have an isotropic or anisotropic orientation for fluid flow. Only the permeability in the *x*-direction is entered when the material is isotropic, while permeabilities in all three Cartesian directions are needed when the material is anisotropic. Therefore, in this work, we computed permeability in the *x*-, *y*-, and *z*-directions due to the intricacy of the porous system of the stromatolite microfacies of Lagoa Salgada.

The basic material information is displayed in Fig. 10(a), where the gray portion represents the matrix and the white portion represents the pores, filled by air. The subvolume of microfacies C has dimensions of 250 × 250 × 250 voxels and a 50 μm scale. Fig. 10(b) shows the fluid flow distribution across the entire pore space of microfacies C. The simulations detected that pore sizes ranged from approximately 0.45 to 204.6 μm.

The permeability values in the *x*-, *y*-, and *z*-directions were 175.84, 192.45, and 115.92 mD, respectively. The mean flow velocities were 163.35, 178.71, and 111.46 m/s in the three directions. Fig. 10(c)–(f) show thin section images of microfacies C.

The relationship between pore size and pressure drop is seen in Fig. 10(g). The pressure drop has a linear behavior in the *x*- and *y*-directions. This occurrence is plausible because the connectivity between the pores in the *x* and *y* directions is more homogeneous compared to the *z* direction, which exhibits a polynomial behavior, as observed in the X-ray images (Fig. 10(h)).

The correlation between the number of iterations required for the algorithm to converge to the mean fluid velocity is depicted in Fig. 10(i). It used 742 iterations in the *x*-direction, 445 in the *y*-direction, and 1516 in the *z*-direction. The larger number of iterations in the z-direction further confirms our idea of how heterogeneous the C microfacies pore system is.

This difference in the pressure drop ratio is related to the coordination network of the pores through which the fluid can travel. In the *z*-direction, the permeability and the fluid velocity are less than in the other directions.

Regarding microfacies B, Fig. 11(a) describes the material distribution, while Fig. 11(b) shows the distribution of sample flow. The permeability values in the *x*-, *y*-, and *z*-directions were 119.39, 276.58, and 209.36 mD, respectively. The mean flow velocities were 106.30, 248.78, and 187.66 m/s in the *x*-, *y*-, and *z*-directions,

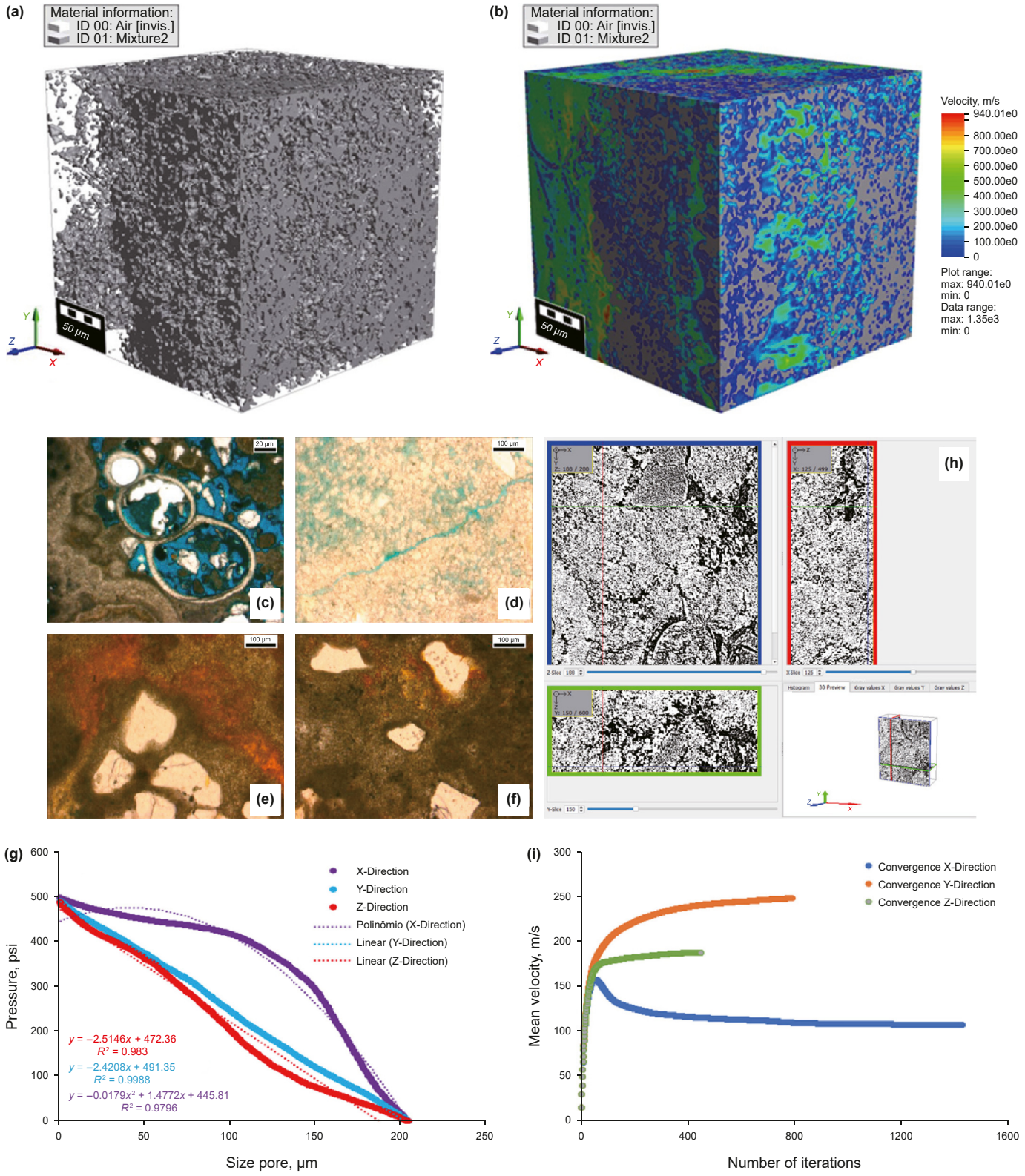

Fig. 10. Description of material information from a sample of the microfacies C, the porous volume of the subvolume used during the simulations **(a)**, the result of simulation of the fluid flow distribution **(b)**, thin sections from the sample where it is possible to observe skeletal material **(c)**, different pore types **(d, e)** and a quartz grain **(f)**, the relationship between pore size and pressure drop in three directions **(g)**, emphasis on the *z*-slice, *x*-slice, *y*-slice, and inline and cross-line slices **(h)**, and the relationship between the number of iterations and mean velocity also in three directions **(i)**.

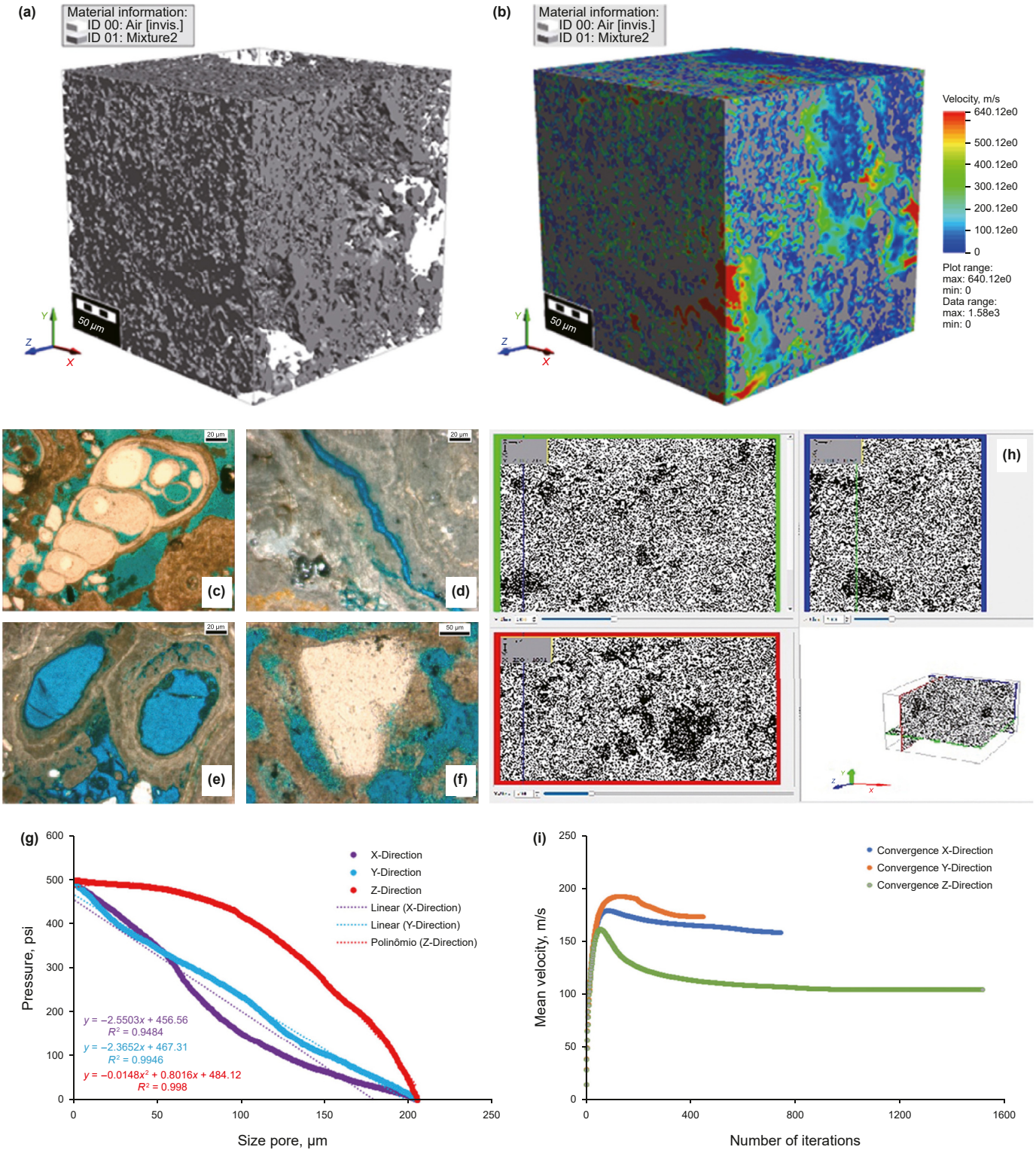

Fig. 11. Description of material information from a sample of the microfacies B. Porous volume of the subvolume used during the simulations **(a)**, result of simulation of the fluid flow distribution **(b)**, thin sections from the sample where it is possible to observe skeletal material **(c)**, small pores and a channel **(d)**, **(e)**, **(f)** quartz grains (white regions) and recrystallization regions (golden regions), the relationship between pore size and pressure drop in three directions **(g)**, emphasis on the *z*-slice, *x*-slice, *y*-slice, and inline and cross-line slices **(h)**, and the relationship between the number of iterations and mean velocity also in three directions **(i)**.

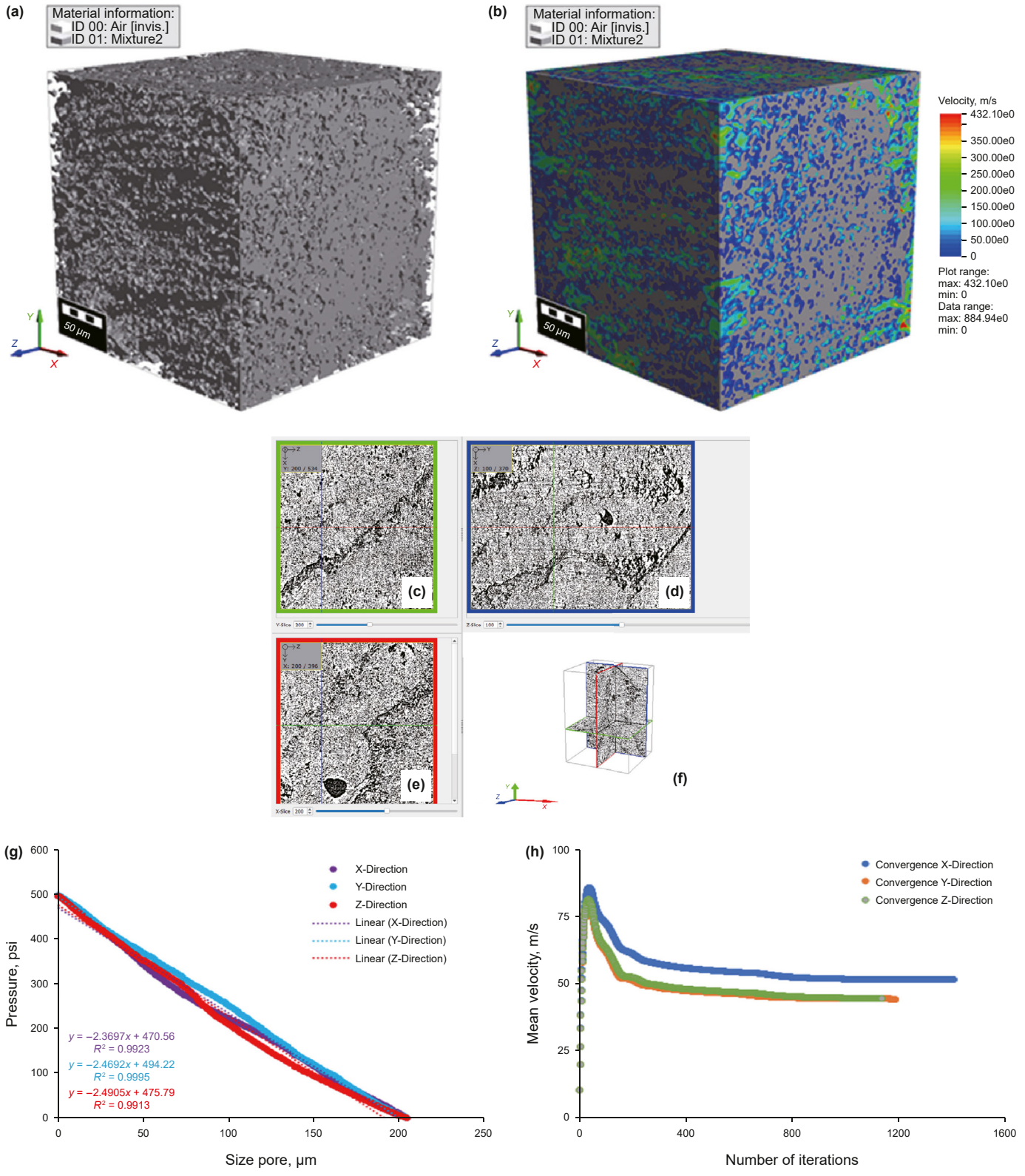

Fig. 12. Description of material information from a sample of the microfacies A. Porous volume of the subvolume used during the simulations **(a)**, the result of simulation of the fluid flow distribution **(b)**, thin sections from the sample where it is possible to observe skeletal material **(c)**, emphasis on the *xz*-slice, *xy*-slice, *yz*-slice, and inline and cross-line slices ((**c**)–(**f**)), the relationship between pore size and pressure drop in three directions **(g)**, and the relationship between the number of iterations and mean velocity also in three directions (**h**).

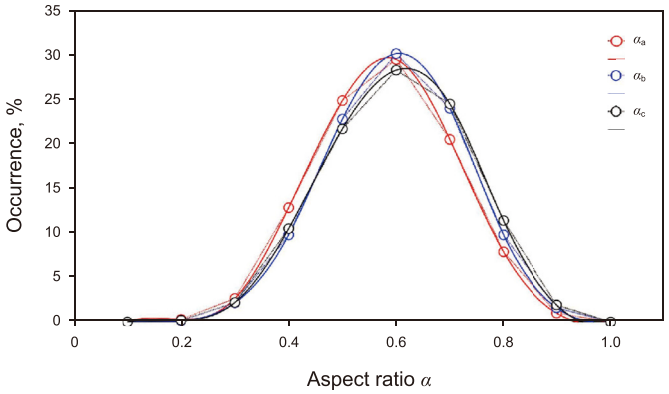

Fig. 13. Pore aspect ratio distribution from DIA according to the processing methods μCT. In red of the microfacies A, in blue of the microfacies B, and black of the microfacies C.

respectively.

Microfacies B thin section images are shown in Fig. 11(c)–(f). The greater number of iterations in the x-direction shows a change in these microfacies' direction and flow velocity (Fig. 11(g)). From the geologic perspective, this is related to the diagenetic deposition processes that occurred during the period of formation of these rocks, as well as the types of microbial structures in the Lagoa Salgada, as viewed in thin section images (Fig. 11(h)). Then, to perform the microfacies B flow simulations, 1426 iterations were required in the *x*-direction, 787 in the *y*-direction, and 448 in the *z*-direction (Fig. 11(i)).

Lastly, Fig. 12(a) and (b) depict the relationship between the matrix, pore space, and flow velocity of microfacies A. In this microfacies, there are no final sections of the sample; therefore, we used only μCT data. Fig. 12(c)–(f) show the μCT slices in planes *XZ*, *XY*, and *YZ*, as well as inline and cross-line slices.

This microfacies presents the best behavior compared to the others, as its characteristics are more homogeneous in the three directions. The homogeneity of microfacies A is notorious when we compare the relationship between the pore size and pressure drop. Note that the fit is linear in all directions, and their equations have a Pearson's correlation coefficient (R^2) greater than 0.99 (Fig. 12(g)).

Microfacies A has the lowest flow velocity (less than 100 m/s) compared to the other microfacies. Consequently, it also has the lowest permeability values in the three directions, i.e., approximately 50 mD. Therefore, to perform the microfacies A flow simulation, the algorithm executed 1404 iterations in the *x*-direction, 1187 in the *y*-direction, and 1138 in the *z*-direction (Fig. 12(h)).

The equations for the trends of the linear and polynomial models, together with their corresponding equations, provide an excellent match in the flow direction in Figs. 10(g), 11(g) and 12(g); in each case, the correlation coefficient is more than 0.94.

The distribution of the pore aspect ratio (α) in microfacies A, B, and C is displayed in Fig. 13, where no discernible variation was seen. With a low standard deviation (about 0.007512) and mean and median aspect ratios of 0.543983 and 0.547326, respectively, the three microfacies show that the majority of their pores are ellipsoids.

The distribution patterns of aspect ratio and gamma (γ) about the diameter of pore size of microfacies A, B, and C are displayed in Fig. 14. The aspect ratio in microfacies A ranges from 0.2 to 0.9, and the pore size diameters are primarily concentrated between 0.5 and 30 μm (Fig. 14(a)). However, the gamma values vary between 1 and 1.25, as this microfacies is the most disorganized and discontinuous, exhibiting a massive character and no lamination (Fig. 14(b)). According to Archilha (2015), worm tubes occur frequently and comprise the macroporosity of these facies, as they are present in the form of circular structures (Table 3).

An increase in pore size diameter in microfacies B is shown in Fig. 14(c). Similar to microfacies A (Fig. 14(d)), the aspect ratio distribution cloud (α) values range from 0.1 to 1, while the gamma distribution cloud (γ) values vary from 1 to 1.4, with an outlier at 1.7. Both microfacies have concentrated pore sizes between 0.5 and 30 μm.

This result occurs because this microfacies has cyclic and crenular laminations of calcium carbonate with a columnar aspect, and the gap between these columns is filled by gastropod shells and worm tubes. The greatest porosity of these microfacies is observed at the top and the interface between microfacies A and B, presenting an intercalation of light brown (presence of phosphate) and reddish brown material. Fenestral porosity is found at the base, at the interface between microfacies B and C, and it develops by following the tops of columnar forms, as the microfacies are very cemented. In addition, the spaces between the columns of the laminations are mainly filled with detrital sediments that are possibly cemented by carbonate (Riding, 2011).

An increase in pore size diameter in microfacies C is shown in Fig. 14(e). The distributions of pore diameters are centered in the range of 0.5–50 μm. As shown in Fig. 14(f), the gamma distribution cloud (γ) values vary from 1 to 1.5, whereas the aspect ratio distribution cloud (α) values are about between 0.15 and 0.95. It happens because this particular microfacies is the most friable; formed by irregular thin layers of calcium, with cavities caused by dissolution.

In microfacies A, approximately 90% of the pores have areas ranging from 50 to 500 μm^2, as shown in Fig. 15(a). The microporosity is around 28%, which aligns with the studies by Anselmetti et al. (1998).

Intermediate microfacies B corresponds to a transition zone between the base and the top of the stromatolite. At the top, at the interface between facies A and B, one can observe the greater porosity of these microfacies and the presence of phosphate (yellow-brown), which replaced the carbonate cement. It presents a behavior similar to that in microfacies A, in which pores with areas between 50 and 500 μm^2 (approximately 72%) also predominate (Fig. 15(b)).

Microfacies C presents a behavior comparable to that of microfacies A, in which pores with areas between 50 and 500 μm^2 predominate (approximately 80%). This microfacies is more porous when compared to microfacies A, and an increase of 4% occurs in relation to the area of micropores and macro-mesopores, and a significant increase in the porosity (image porosity) occurs, increasing from 28.2584% to 35.9323% (Fig. 15(c)).

The solver run time used in the simulations of the three microfacies was approximately 66.3068 h to process 324671793 cells with 47.632 GB of used computational memory, operated by a Windows 64-bit operating system. Table 4 shows a summary of the properties estimated for the three microfacies.

6. Conclusions

This study's primary goal was to assess the petrophysical characteristics and fluid flow in samples from a Brazilian stromatolite outcrop located in Lagoa Salgada, Rio de Janeiro, which is known to be analogous to Brazilian pre-salt reservoirs. The study focused on

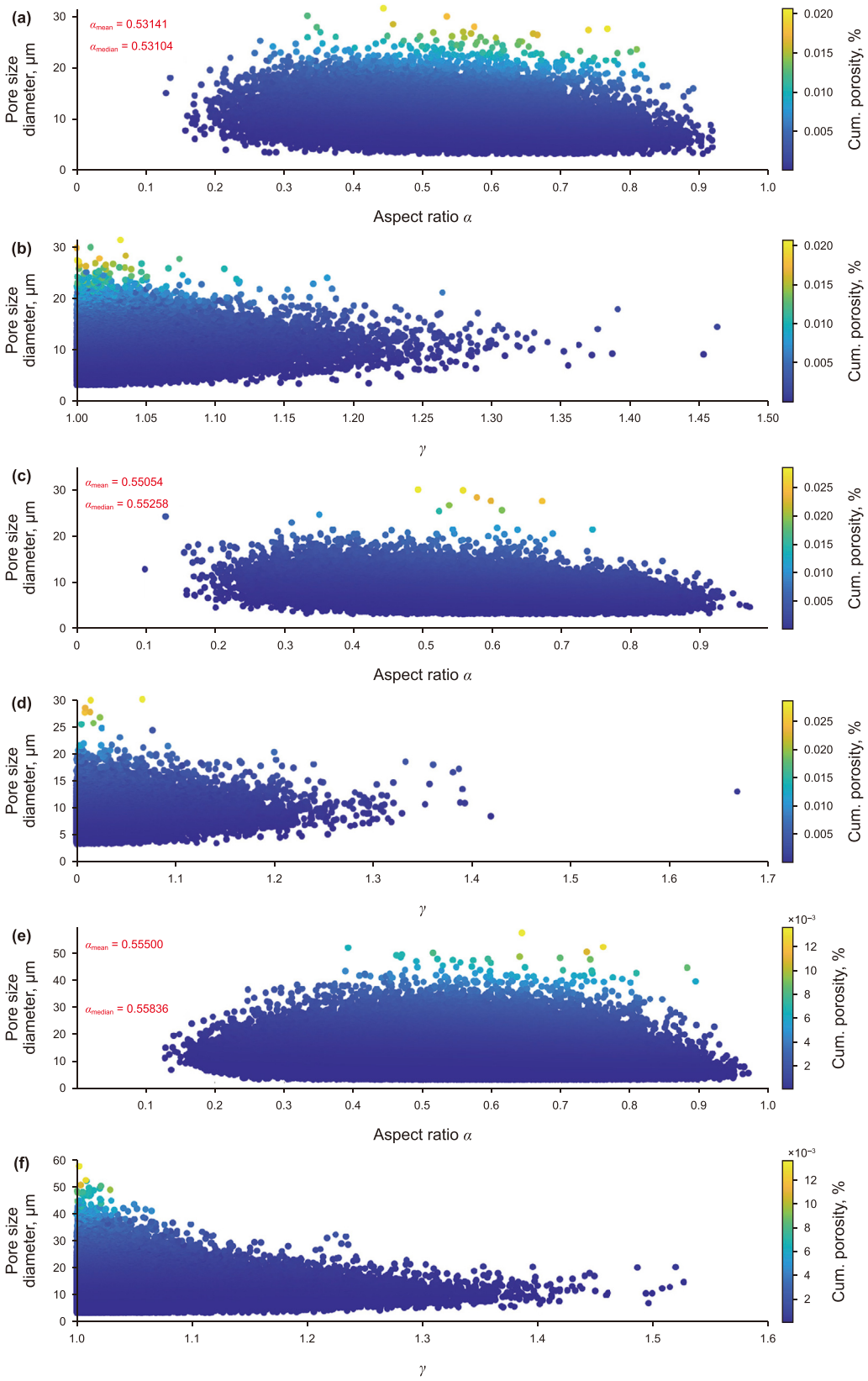

Fig. 14. Correlation between the local parameters and the pore size diameter of microfacies A, B, and C; top ((**a**), (**b**)), center ((**c**), (**d**)), and bottom ((**e**), (**f**)).

Table 3
Local parameters of the porous space of microfacies A, B, and C.

Microfacies	α_{mean}	α_{median}	γ
A	0.53141	0.53104	1.035
B	0.55054	0.55258	1.031
C	0.55000	0.55836	1.031

estimating rock properties using digital imaging and analysis (DIA) techniques from large-volume micro-CT images.

Emphasis was placed on balancing the acquisition of accurate 3D micro-CT sub-volume results while maintaining image resolution. The watershed image segmentation algorithm proved effective in filtering images and analyzing matrix-pore relationships. The simulations were necessary to comprehensively understand the porous media system of the samples and model fluid flow in the reservoir.

The results indicated connected pores in the core sample, particularly evident in two microfacies. Microfacies C exhibited laminar fluid flow in the *x* and *y* directions, while the *z*-direction suggested possible turbulent flow. Microfacies B showed laminar fluid flow in the *y* and *z* directions and turbulent flow in the *x* direction. Microfacies A had a more homogeneous pore system, as shown in equations that relate pressure versus pore size. This heterogeneity in fluid flow simulations is directly related to the depositional environment of stromatolites, highlighting the connectivity of this complex pore system.

Aspect ratio describes the shape of pores within rocks, regardless of their size, and can be consistent across both large and small pores. This relative geometric measurement allows for uniform characterization of pore systems, along with the gamma parameter. No significant variation in aspect ratio was observed across the three microfacies, despite differences in pore size diameter.

The analysis of fluid flow within complex pore systems in carbonate reservoirs necessitates robust simulation tools and mathematical foundations. The Navier-Stokes equation provides a comprehensive framework for describing fluid flow properties in such intricate systems. The solver used in this study demonstrated significant robustness in estimating rock properties from pore morphology, showcasing its independence from the boundary conditions of the Navier-Stokes equation. This indicates the solver's reliability and versatility in various simulation scenarios, reinforcing its effectiveness for reservoir characterization and fluid flow modeling.

Another factor that influences the change of direction of flow fluid is diagenetic cementation. Regions with heavy cementation might act as barriers to flow (microfacies A), while less cemented areas might still permit fluid passage. The formation of this diagenetic cement can block or partially obstruct existing flow pathways, forcing fluids to reroute (microfacies B and C). This can lead to the development of preferential flow channels, where fluid moves more easily through less cemented regions, and can cause non-uniform fluid distribution, complicating the modeling and prediction of fluid movement within the stromatolite during the

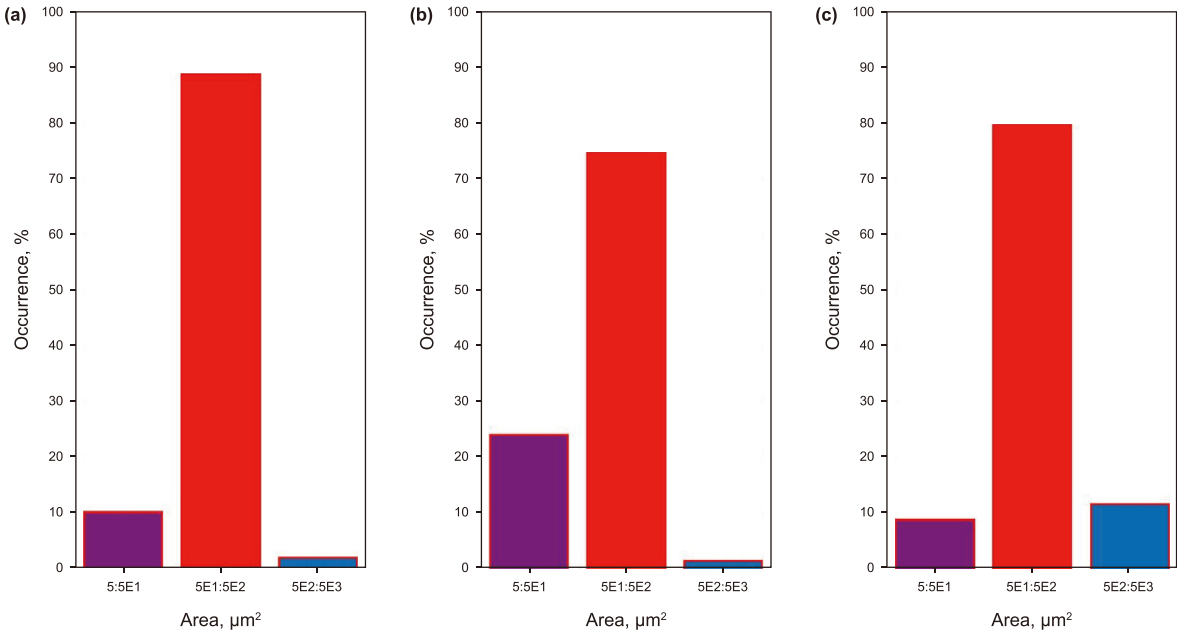

Fig. 15. Quantitative characterization of pore area by digital image analysis to according Anselmetti et al. (1998).

Table 4
Schematic summary of the estimated flow properties in the three directions of the stromatolite of the Lagoa Salgada.

Properties	Direction	Microfacies A	Microfacies B	Microfacies C
Permeabilitiy, mD	*X*	57.37	119.39	175.87
	Y	49.52	276.58	192.45
	Z	49.93	209.36	115.92
Estimated average velocity, m/s	*X*	51.71	106.30	158.60
	Y	44.36	248.78	172.31
	Z	44.93	187.66	162.97

simulation.

Using sub-volumes with cubic dimensions for large images or limited computing capacity is recommended. The selection of geomechanical parameters for Lagoa Salgada stromatolites ensured simulation quality and reliable rock property trends. The study successfully validated a continuous flow system between microfacies by analyzing the pressure drop, mean velocity, and changes in flow direction.

The practical value of this study lies in its potential to enhance reservoir characterization, improve simulation accuracy, mitigate risks, drive technology development, and increase cost efficiency in oil and gas exploration.

CRediT authorship contribution statement

Herson Oliveira da Rocha: Writing – review & editing, Writing – original draft, Visualization, Validation, Supervision, Software, Resources, Project administration, Methodology, Investigation, Funding acquisition, Formal analysis, Data curation, Conceptualization. **Roseane Marchezi Missagia:** Writing – review & editing, Writing – original draft, Visualization, Supervision, Resources, Project administration, Methodology, Investigation, Funding acquisition, Formal analysis, Data curation, Conceptualization. **Marco Antonio Rodrigues de Ceia:** Writing – review & editing, Writing – original draft, Visualization, Validation, Supervision, Resources, Project administration, Investigation, Funding acquisition, Data curation, Conceptualization. **André Oliveira Martins:** Writing – review & editing, Writing – original draft, Visualization, Validation, Software, Methodology, Investigation, Formal analysis, Conceptualization. **Rafaella Rocha Baggieri:** Writing – original draft, Visualization, Methodology, Investigation, Formal analysis, Conceptualization. **Irineu de Azevedo Lima Neto:** Writing – review & editing, Writing – original draft, Visualization, Validation, Supervision, Software, Methodology, Investigation, Formal analysis, Data. **Lucas Cesar Oliveira:** Visualization, Validation, Supervision, Resources, Investigation, Funding acquisition, Formal analysis, Data curation, Conceptualization, Writing – original draft, Visualization, Validation, Software, Methodology, Investigation, Formal analysis, Data curation.

Declaration of competing interest

The authors declare that they have no known competing financial interests or personal relationships that could have appeared to influence the work reported in this paper. The authors also declare the absence of any conflict of interest and affirm that this manuscript is not being published, either partially or in full, in any other periodical, as it is being submitted exclusively to this journal.

Acknowledgment

The authors thank UENF/LENEP for all the environment and structure provided to execute this work. This study was financed in part by the Coordenação de Aperfeiçoamento de Pessoal de Nível Superior of the Ministry of Education (CAPES/MEC/BRAZIL)-Finance Code 001, Equinor Energy of Brazil Company (Project No. 4600025270), the Brazilian National Agency of Petroleum, Gas, and Biofuels (ANP), and Petrobras (Project No. 46000579151). MC and RM thank INCT/Petroleum Geophysics for financial support; and the National Council for Scientific and Technological Development (CNPq) for their Research Grants of Productivity in Technological Development and Innovation-DT II (313522/2019-7 and 313746/2019-2).

References

Abe, H., 2017. Reynolds-number dependence of wall-pressure fluctuations in a pressure-induced turbulent separation bubble. J. Fluid Mech. 833, 563–598. https://doi.org/10.1017/jfm.2017.694.

Abrahão, D., Warme, J.E., 1990. Lacustrine and Associated Deposits in a Rifted Continental Margin-Lower Cretaceous Lagoa Feia Formation, Campos Basin, Offshore Brazil. American Association of Petroleum Geologists, Memoir 50, 287–305.

Ahr, W.M., 2008. Geology of carbonate reservoirs: the Identification. Description, and Characterization of Hydrocarbon Reservoirs in Carbonate Rocks. John Wiley & Sons, p. 296.

Alpak, F.O., Gray, F., Saxena, N., Dietderich, J., Hofmann, R., Berg, S., 2018. A distributed parallel multiple-relaxation-time lattice Boltzmann method on general-purpose graphics processing units for the rapid and scalable computation of absolute permeability from high-resolution 3D micro-CT images. Comput. Geosci. 22, 815–832. https://doi.org/10.1007/s10596-018-9727-7.

Alvarenga, R.D.S., Kuchle, J., Iacopini, D., Goldberg, K., Scherer, C.M.D.S., Pantopoulos, G., Ene, P.L., 2021. Tectonic and stratigraphic evolution based on seismic sequence stratigraphy: central rift section of the Campos Basin, offshore Brazil. Geosciences 11 (8), 338. https://doi.org/10.3390/geosciences11080338.

Anselmetti, F.S., Luthi, S., Eberli, G.P., 1998. Quantitative characterization of carbonate pore systems by digital image analysis. AAPG (Am. Assoc. Pet. Geol.) Bull. 82 (10), 1815–1836.

Archilha, N.L., 2015. Quantification of geometric parameters of the porous system by X-ray tomography and analysis of the influence on physical properties of carbonate rocks. Ph. D. thesis. Universidade Estadual do Norte Fluminense Darcy Ribeiro, Campos dos Goytacazes, Brazil.

Archilha, N., Missagia, R., de Ceia, M., Neto, I.L., 2013. Petrophysical, mineralogical and elastic property characterization of Halocene carbonates from Salgada lagoon, Brazil. In: SEG International Exposition and Annual Meeting.

Archilha, N.L., Missagia, R.M., Hollis, C., D, et al., 2016. Permeability and acoustic velocity controlling factors determined from X-ray tomography images of carbonate rocks. AAPG Bulletin 100 (8), 1289–1309.

Asquith, G.B., Gibson, C.R., 1982. Basic well-log analysis for geologists, 2. American Association of Petroleum Geologists, Tulsa, Oklahoma.

Austin Jr, J.A., Uchupi, E., 1982. Continental-oceanic crustal transition off southwest africa. AAPG (Am. Assoc. Pet. Geol.) Bull. 66 (9), 1328–1347. https://doi.org/10.1306/03B5A79B-16D1-11D7-8645000102C1865D.

Brelaz, L.C., Ribeiro, M.G.S., Borghi, L., 2017. Análise Petrográfica e Petrofísica de Calcários Análogos aos Reservatórios Microbiais do Pré-sal. In: 15th International Congress of the Brazilian Geophysical Society & EXPOGEF, Rio de Janeiro, Brazil, 31 July-3 August 2017. Brazilian Geophysical Society, pp. 921–926. https://doi.org/10.1190/sbgf2017-180.

Brigaud, B., Vincent, B., Durlet, C., Deconinck, J.F., Jobard, E., Pickard, N., Yven, B., Landrein, P., 2014. Characterization and origin of permeability–porosity heterogeneity in shallow-marine carbonates: from core scale to 3D reservoir dimension (Middle Jurassic, Paris Basin, France). Mar. Petrol. Geol. 57, 631–651. https://doi.org/10.1016/j.marpetgeo.2014.07.004.

Brown, J.M., 2015. Determination of Hashin–Shtrikman bounds on the isotropic effective elastic moduli of polycrystals of any symmetry. Comput. Geosci. 80, 95–99. https://doi.org/10.1016/j.cageo.2015.03.009.

Cainelli, C., Mohriak, W.U., 1999. Some remarks on the evolution of sedimentary basins along the Eastern Brazilian continental margin. Episodes Journal of International Geoscience 22 (3), 206–216. https://doi.org/10.18814/epiiugs/1999/v22i3/008.

Carminatti, M., Dias, J., Wolff, B., 2009. From turbidites to carbonates: breaking paradigms in deep waters. In: Offshore Technology Conference, OTC-20124. https://doi.org/10.4043/20124-MS.

Ceia, M., Missagia, R., Archilha, N., Baggieri, R., Santos, V., Fidelis, S., Lima Neto, I., 2022. Petrophysical characterization of Lagoa Salgada stromatolites - a Brazilian pre-salt analog. J. Petrol. Sci. Eng. 218, 111012. https://doi.org/10.1016/j.petrol.2022.111012.

Chafetz, H.S., 2013. Porosity in bacterially induced carbonates: focus on micropores. AAPG (Am. Assoc. Pet. Geol.) Bull. 97 (11), 2103–2111. https://doi.org/10.1306/04231312173.

Chinelatto, G.F., Belila, A.M.P., Basso, M., Souza, J.P.P., Vidal, A.C., 2020. A taphofacies interpretation of shell concentrations and their relationship with petrophysics: a case study of Barremian-Aptian coquinas in the Itapema Formation, Santos Basin-Brazil. Mar. Petrol. Geol. 116, 104317. https://doi.org/10.1016/j.marpetgeo.2020.104317.

Chinelatto, G.F., Belila, A.M.P., Basso, M., Vidal, A.C., 2021. Relationship between biofabric and petrophysics in coquinas, insights on Brazilian Barremian-Aptian carbonates of the Santos and Sergipe-Alagoas Basins. Int. J. Earth Sci. 110, 2597–2617. https://doi.org/10.1007/s00531-020-01948-z.

Choquette, P.W., Pray, L.C., 1970. Geologic nomenclature and classification of porosity in sedimentary carbonates. AAPG (Am. Assoc. Pet. Geol.) Bull. 54 (2), 207–250. https://doi.org/10.1306/5D25C98B-16C1-11D7-8645000102C1865D.

Coleman, G.N., Rumsey, C.L., Spalart, P.R., 2018. Numerical study of turbulent separation bubbles with varying pressure gradient and Reynolds number. J. Fluid Mech. 847, 28–70. https://doi.org/10.1017/jfm.2018.257.

Da Wang, Y., Chung, T., Armstrong, R.T., McClure, J.E., Mostaghimi, P., 2019. Computations of permeability of large rock images by dual grid domain decomposition. Adv. Water Resour. 126, 1–14. https://doi.org/10.1016/

j.advwatres.2019.02.002.
De Oliveira, V.C.B., de Assis Silva, C.M., Borghi, L.F., de Souza Carvalho, I., 2019. Lacustrine coquinas and hybrid deposits from rift phase: pre-Salt, lower Cretaceous, Campos Basin, Brazil. J. S. Am. Earth Sci. 95, 102254. https://doi.org/10.1016/j.jsames.2019.102254.
Ehrenberg, S.N., Eberli, G.P., Keramati, M., Moallemi, S.A., 2006. Porosity-permeability relationships in interlayered limestone-dolostone reservoirs. AAPG (Am. Assoc. Pet. Geol.) Bull. 90 (1), 91–114. https://doi.org/10.1306/08100505087.
Ehrenberg, S.N., Walderhaug, O., Bjørlykke, K., 2012. Carbonate porosity creation by mesogenetic dissolution: reality or illusion? AAPG (Am. Assoc. Pet. Geol.) Bull. 96 (2), 217–233. https://doi.org/10.1306/05031110187.
Faroughi, S.A., Roriz, A.I., Fernandes, C., 2022. A meta-model to predict the drag coefficient of a particle translating in viscoelastic fluids: a machine learning approach. Polymers 14 (3), 430. https://doi.org/10.3390/polym14030430.
Gerdes, G., Claes, M., Dunajtschik-Piewak, K., Riege, H., Krumbein, W.E., Reineck, H.E., 1993. Contribution of microbial mats to sedimentary surface structures. Facies 29, 61–74. https://doi.org/10.1007/BF02536918.
Herlinger Jr, R., Freitas, G.D.N., dos Anjos, C.D.W., De Ros, L.F., 2020. Petrological and petrophysical implications of magnesian clays in Brazilian pre-salt deposits. In: SPWLA Annual Logging Symposium. SPWLA. https://doi.org/10.30632/SPWLA-5004.
Kong, L., Ostadhassan, M., Li, C., Tamimi, N., 2018. Pore characterization of 3D-printed gypsum rocks: a comprehensive approach. J. Mater. Sci. 53, 5063–5078. https://doi.org/10.1007/s10853-017-1953-1.
Korchinski, M., Teyssier, C., Rey, P.F., Whitney, D.L., Mondy, L., 2021. Single-phase vs two-phase rifting: numerical perspectives on the accommodation of extension during continental break-up. Mar. Petrol. Geol. 123, 104715. https://doi.org/10.1016/j.marpetgeo.2020.104715.
Leavline, E.J., Singh, D.A.A.G., 2014. On teaching digital image processing with MATLAB. Am. J. Signal Process. 7–15. https://doi.org/10.5923/j.ajsp.20140401.02.
Leighton, M.W., Pendexter, C., 1962. Carbonate rock types. In: Ham, W.E. (Ed.), Classification of carbonate rocks. American Association of Petroleum Geologists Memoir, pp. 33–61.
Lima, B.E.M., De Ros, L.F., 2019. Deposition, diagenetic, and hydrothermal processes in the Aptian Pre-Salt lacustrine carbonate reservoirs of the northern Campos Basin, offshore Brazil. Sediment. Geol. 383, 55–81. https://doi.org/10.1016/j.sedgeo.2019.01.006.
Lima Neto, I.A., Ceia, M.A., Misságia, R.M., Oliveira, G.L., Santos, V.H., Paranhos, R.P., Archilha, N.L., 2018. Testing and evaluation of 2D/3D digital image analysis methods and inclusion theory for microporosity and S-wave prediction in carbonates. Mar. Petrol. Geol. 97, 592–611. https://doi.org/10.1016/j.marpetgeo.2018.08.004.
Linden, S., Wiegmann, A., Hagen, H., 2015. The LIR space partitioning system applied to the Stokes equations. Graph. Model. 82, 58–66. https://doi.org/10.1016/j.gmod.2015.06.003.
Linden, S. Planas, Wiegmann, A., Cheng, L., 2018. FlowDict user guide. Release 2018 [Online]. Available: https://www.geodict.com/Support/UserGuide.php.
Lønøy, A., 2006. Making sense of carbonate pore systems. AAPG (Am. Assoc. Pet. Geol.) Bull. 90, 1382–1405. https://doi.org/10.1306/03130605104.
Lv, A., Cheng, L., Aghighi, M.A., Masoumi, H., Roshan, H., 2021. A novel workflow based on physics-informed machine learning to determine the permeability profile of fractured coal seams using downhole geophysical logs. Mar. Petrol. Geol. 131, 105171. https://doi.org/10.1016/j.marpetgeo.2021.105171.
Mahmoud, N.P., Zabihi, A., 2017. Numerical simulation of a single-phase flow through fractures with permeable, porous and non-ductile walls. Eng. Technol. Appl. Sci. Res. 7 (5), 2041–2046. https://doi.org/10.48084/etasr.1448.
Moreira, J.L.P., Madeira, C.V., Gil, J.A., Machado, M.A.P., 2007. Bacia de Santos. Bol. Geociencias Petrobras 15 (2), 531–549.
Nürnberg, D., Müller, R.D., 1991. The tectonic evolution of the South atlantic from late jurassic to present. Tectonophysics 191 (1–2), 27–53. https://doi.org/10.1016/0040-1951(91)90231-G.
Oliveira, L., Martins, A., Ceia, M., Misságia, R., Rocha, H., Santarém, N., Lima Neto, I., 2022. Comparative analysis between laboratory measurement and numerical simulation to evaluate anisotropy in Coquinas from Morro do Chaves Formation: a Brazilian pre-salt analog. In: SEG/AAPG International Meeting for Applied Geoscience & Energy. OnePetro. https://doi.org/10.1190/image2022-3751590.1.
Otsu, N., 1979. A threshold selection method from gray-level histograms. IEEE Transactions on Systems, Man, and Cybernetics 9 (1), 62–66.
Proctor, J.M., Droxler, A.W., Derzhi, N., Hopson, H.H., Harris, P.M., Khanna, P., Lehrmann, D.J., 2019. Upscaling lithology and porosity-type fractions from the micro-to the core-scale with thin-section petrography, dual-energy computed tomography, and rock typing: creation of diagenesis and porosity-type logs. Interpretation 7 (1), B9–B32. https://doi.org/10.1190/INT-2017-0187.1.
Rabbani, A., Ayatollahi, S., 2015. Comparing three image processing algorithms to estimate the grain-size distribution of porous rocks from binary 2D images and sensitivity analysis of the grain overlapping degree. Spec. Top Rev. Porous Media Int. J. 6 (1). https://doi.org/10.1615/SpecialTopicsRevPorousMedia.v6.i1.60.
Rabbani, A., Ayatollahi, S., Kharrat, R., Dashti, N., 2016. Estimation of 3-D pore network coordination number of rocks from watershed segmentation of a single 2-D image. Adv. Water Resour. 94, 264–277. https://doi.org/10.1016/j.advwatres.2016.05.020.
Rabinowitz, P.D., Labrecque, J., 1979. The mesozoic South Atlantic ocean and evolution of its continental margins. J. Geophys. Res. Solid Earth 84 (B11), 5973–6002. https://doi.org/10.1029/JB084iB11p05973.
Rezende, M.F., Tonietto, S.N., Pope, M.C., 2013. Three-dimensional pore connectivity evaluation in a Holocene and jurassic microbialite buildup three-dimensional pore connectivity evaluation in microbialite buildup. AAPG (Am. Assoc. Pet. Geol.) Bull. 97 (11), 2085–2101. https://doi.org/10.1306/05141312171.
Ricardi-Branco, F., Callefo, F., Cataldo, R.A., Noffke, N., Pessenda, L.C.R., Vidal, A.C., Branco, F.C., 2018. Microbial biofacies and the influence of metazoans in Holocene deposits of the Lagoa Salgada, Rio de Janeiro state, Brazil. J. Sediment. Res. 88 (11), 1300–1317. https://doi.org/10.2110/jsr.2018.64.
Riding, R., 2011. Microbialites, stromatolites, and thrombolites. In: Reitner, J., Thiel, V. (Eds.), Encyclopedia of Geobiology. Encyclopedia of Earth Sciences Series. Springer, Dordrecht. https://doi.org/10.1007/978-1-4020-9212-1_196.
Riding, R., Liang, L., 2005. Geobiology of microbial carbonates: metazoan and seawater saturation state influences on secular trends during the Phanerozoic. Paleogeography, Paleoclimatology, Paleoecology 219, 101–115. https://doi.org/10.1016/j.palaeo.2004.11.018.
Saller, A., Rushton, S., Buambua, L., Inman, K., Mcneil, R., Dickson, J.T., 2016. Pre-salt stratigraphy and depositional systems in the Kwanza Basin, offshore Angola. AAPG (Am. Assoc. Pet. Geol.) Bull. 100 (7), 1135–1164. https://doi.org/10.1306/02111615216.
Saxena, N., Mavko, G., 2016. Estimating elastic moduli of rocks from thin sections: digital rock study of 3D properties from 2D images. Comput. Geosci. 88, 9–21. https://doi.org/10.1016/j.cageo.2015.12.008.
Saxena, N., Hofmann, R., Alpak, F.O., Berg, S., Dietderich, J., Agarwal, U., Wilson, O.B., 2017. References and benchmarks for pore-scale flow simulated using micro-CT images of porous media and digital rocks. Adv. Water Resour. 109, 211–235. https://doi.org/10.1016/j.advwatres.2017.09.007.
Saxena, N., Hows, A., Hofmann, R., Alpak, F.O., Freeman, J., Hunter, S., Appel, M., 2018. Imaging and computational considerations for image computed permeability: operating envelope of digital rock physics. Adv. Water Resour. 116, 127–144. https://doi.org/10.1016/j.advwatres.2018.04.001.
Saxena, N., Hows, A., Hofmann, R., Alpak, F.O., Dietderich, J., Appel, M., De Jong, H., 2019. Rock properties from micro-CT images: digital rock transforms for resolution, pore volume, and field of view. Adv. Water Resour. 134, 103419. https://doi.org/10.1016/j.advwatres.2019.103419.
Schmidt, T., Schimmer, F., Widera, A., May, D., Motsch, N., Bauer, C., 2019. A novel simulative-experimental approach to determine the permeability of technical textiles. Key Eng. Mater. 809, 487–492. https://doi.org/10.4028/www.scientific.net/KEM.809.487.
Silva, D.R.D., Mansur, K.L., Borghi, L., 2018. Evaluation of the scientific value of Lagoa Salgada (Rio de Janeiro, Brazil): characterization as geological heritage, threats and strategies for geoconservation. Journal of the Geological Survey of Brazil 1 (2), 69–80. https://doi.org/10.29396/jgsb.2018.v1.n2.2.
Simões Maciel, R., Ressel Pereira, F.D., Fieni Fejoli, R., Leibsohn Martins, A., Duarte Ferreira, M.V., 2019. Enhancing scale prediction in pre-salt wells using numerical simulation. In: SPE Annual Technical Conference and Exhibition. https://doi.org/10.2118/196180-ms.
Soltanmohammadi, R., Iraji, S., de Almeida, T.R., Basso, M., Munoz, E.R., Vidal, A.C., 2024. Investigation of pore geometry influence on fluid flow in heterogeneous porous media: a pore-scale study. Energy Geoscience 5 (1), 100222. https://doi.org/10.1016/j.engeos.2023.100222.
Srivastava, N.K., Schobbenhaus, C., Campos, D.A., Queiroz, E.T., Winge, M., Berbert-Born, M., 1999. Lagoa Salgada (Rio de Janeiro): Recent Stromatolites. Geological and Paleontological Sites of Brazil: DNPM/CPRM - Brazilian Commission of Geological and Paleobiological Sites (SIGEP) 1, 203–209 (in Portuguese).
Sternai, P., Muller, V.A.P., Jolivet, L., Garzanti, E., Corti, G., Pasquero, C., Faccenna, C., 2021. Effects of asthenospheric flow and orographic precipitation on continental rifting. Tectonophysics 820, 229120. https://doi.org/10.1016/j.tecto.2021.229120.
Tahmasebi, P., Javadpour, F., Sahimi, M., Piri, M., 2016. Multiscale study for stochastic characterization of shale samples. Adv. Water Resour. 89, 91–103. https://doi.org/10.1016/j.advwatres.2016.01.008.
Thompson, D.L., Stilwell, J.D., Hall, M., 2015. Lacustrine carbonate reservoirs from early cretaceous rift lakes of western gondwana: pre-salt coquinas of Brazil and west africa. Gondwana Res. 28 (1), 26–51. https://doi.org/10.1016/j.gr.2014.12.005.
Tropea, C., Yarin, A.L., Foss, J.F., 2007. In: Springer handbook of experimental fluid mechanics. Springer, Berlin, p. 237. https://doi.org/10.1007/978-3-540-30299-5.
Tsuchiyama, A., Uesugi, M., Matsushima, T., Michikami, T., Kadono, T., Nakamura, T., Kawaguchi, J., 2011. Three-dimensional structure of Hayabusa samples: origin and evolution of Itokawa regolith. Science 333 (6046), 1125–1128. https://doi.org/10.1126/science.120780.
van Lopik, J.H., Snoeijers, R., van Dooren, T.C., Raoof, A., Schotting, R.J., 2017. The effect of grain size distribution on nonlinear flow behavior in sandy porous media. Transport Porous Media 120, 37–66. https://doi.org/10.1007/s11242-017-0903-3.
Wiegmann, A., Iliev, O., Schindelin, A., 2010. Computer aided engineering of filter materials and pleated filters. Global Guide of the Filtration and Separation Industry 191–198.
Winter, W.R., Jahnert, R.J., França, A.B., 2007. Bacia de Campos. Bol. Geociencias Petrobras 15 (2), 511–529 (in Portuguese).
Wright, V.P., 2012. Lacustrine carbonates in rift settings: the interaction of volcanic and microbial processes on carbonate deposition. Geological Society, London, Special Publications 370 (1), 39–47. https://doi.org/10.1144/SP370.2.

Wright, V.P., Barnett, A.J., 2015. An abiotic model for the development of textures in some South Atlantic early Cretaceous lacustrine carbonates. Geol. Soc. Lond. Spec. Publ. 418 (1), 209–219. https://doi.org/10.1144/sp418.3.
Zhang, L., Jing, W., Yang, Y., Yang, H., Guo, Y., Sun, H., Yao, J., 2019. The investigation of permeability calculation using digital core simulation technology. Energies 12 (17), 3273. https://doi.org/10.3390/en12173273.
Zhu, D., Liu, Q., He, Z., Ding, Q., Wang, J., 2020. Early development and late preservation of porosity linked to presence of hydrocarbons in Precambrian microbialite gas reservoirs within the Sichuan Basin, southern China. Precambrian Res. 342, 105694. https://doi.org/10.1016/j.precamres.2020.105694.